AIAA 2017-3520

AIAA AVIATION Forum
5-9 June 2017, Denver, Colorado
23rd AIAA/CEAS Aeroacoustics Conference

Preliminary Investigation of Multilobe Fighter Jet Noise Sources Using Acoustical Holography[1]

Alan T. Wall[2]
Air Force Research Laboratory, Wright-Patterson Air Force Base, OH 45433, USA

Kevin M. Leete,[3] Kent L. Gee,[4] and Tracianne B. Neilsen[5]
Brigham Young University, Provo, UT 84602, USA

Michael M. James[6]
Blue Ridge Research and Consulting, Asheville, NC 28801, USA

and

Richard L. McKinley[7]
Air Force Research Laboratory, Wright-Patterson Air Force Base, OH 45433, USA

An understanding of jet noise source mechanisms can facilitate targeted noise reduction efforts. This understanding has been enhanced with acoustic imaging technologies, such as near-field acoustical holography (NAH). In this study, multisource statistically optimized NAH (M-SONAH) was used to image the sound field near a tethered F-35 aircraft at multiple frequencies. A linear microphone array, placed along the ground, spanned the length of the jet exhaust plume. A multisource model of the sound field was included in the algorithm to incorporate the effects of the ground reflection on the measurement. Narrowband reconstructions elucidated fine details of the radiation patterns, such as multilobe radiation patterns (which may supersede "dual-lobe" patterns shown in previous studies), and broadband shock-associated noise. [Work supported by F-35 JPO.]

Nomenclature

$\mathbf{A}$	hologram wave function total matrix	$\mathbf{p}$	complex pressure vector
$\mathbf{B}$	hologram wave function submatrix	$\mathbf{r}$	cylindrical coordinate vector
H	Hermitian transpose	$\mathbf{r}_h$	hologram location vector
$H_\ell^{(1)}$	Hankel function	$\mathbf{r}_q$	reconstruction location vector
i	imaginary unit	r, ϕ, z	cylindrical coordinates
k	acoustic wavenumber	r_0	reference radius
k_r	radial wavenumber	$\mathbf{R}_{\mathbf{A}^\mathrm{H}\mathbf{A}}$	regularized inverse of $\mathbf{A}^\mathrm{H}\mathbf{A}$
k_z	axial wavenumber	T	transpose operator
L_z	axial aperture length	x,y,z	Cartesian coordinates
ℓ	order of Hankel function	$\boldsymbol{\alpha}$	reconstruction wave function total matrix

---

[1] Distribution A: Approved for public release; distribution unlimited. Cleared 03/23/2017; JSF17-357.

[2] Corresponding Author, Research Physicist, Battlespace Acoustics Branch, 2610 Seventh St., Bldg. 441, Wright-Patterson AFB, OH 45433, AIAA Member.

[3] Graduate Student, Dept. of Physics and Astronomy, N283 ESC, Provo, UT 84602, AIAA Student Member.

[4] Associate Professor, Dept. of Physics and Astronomy, N283 ESC, Provo, UT 84602, AIAA Senior Member.

[5] Part-time Professor, Dept. of Physics and Astronomy, N283 ESC, Provo, UT 84602, AIAA Member.

[6] Vice President and Senior Principal Engineer, 29 N Market St., Suite 700, Asheville, NC 28801, AIAA Member.

[7] F-35 Joint Program Office, Specialty Engineering – Acoustics Lead, 2610 Seventh St., Bldg. 441, Wright-Patterson AFB, OH 45433.

$\boldsymbol{\beta}$	reconstruction wave function submatrix	Φ	cylindrical wave function
θ	radiation angle wrt jet engine inlet axis		

I. Introduction

HIGH-RESOLUTION acoustic modeling of full-scale supersonic jet engines is a key tool for identifying the sources to be targeted in jet-noise reduction strategies. Laboratory-scale data is critical but may be insufficient because some source behaviors and noise prediction models are difficult to scale up with the precision necessary to inform full-scale engine design decision criteria. Near-field acoustical holography (NAH) was developed for three-dimensional imaging of noise sources,[1,2] and it has been used to characterize both laboratory-scale[3,4,5] and full-scale jet noise.[6,7] NAH is applied here to reconstruct an equivalent acoustic source model and radiated sound field properties of an F-35. The narrowband reconstructions provide insights into the frequency-dependent variations in the sound radiation as well as insights into the multilobed directivity observed in previous studies.[7,8,9,10] The development of next-generation engines for tactical military jet aircraft can benefit from targeted noise source reduction during the design phases.

Many efforts to produce an equivalent source model for jet noise has focused on the noise in the dominant radiation lobe. Mollo-Christensen[11] observed correlated regions in the sound near jet flows as early as 1967 and modeled them with analytical functions that represented a spatially correlated source with a characteristic wave number, phase speed, and amplitude modulation (downstream growth and decay). These properties have become tenets of jet noise modeling efforts. Tam[12] linked the dominant directional acoustic radiation to the growth and decay of instability waves in the jet shear layer. Tam[13] also proposed that the relation between the peak radiation direction and the source phase speed is the same as the relation between the direction of Mach wave radiation and the speed of a supersonically traveling wavy wall. The narrowband NAH imaging efforts of the F-35 noise support many of these ideas but also provide evidence that there are additional features, such as multilobe radiation, in full-scale jet noise that need to be explained.

Multilobe radiation is a seemingly ubiquitous feature of full-scale jets[14,15,16] that has recently received increased attention.[8,9] Although no conclusive explanation of multilobe radiation has been given, its origins are being investigated. At least as early as 1992, Seiner *et al*. identified multiple "families" of Mach waves in high-temperature jets, with varying convective velocities. Tam and Parrish[17] sought to explain multiple spectral peaks shown in prior one-third octave (OTO) band spectra[9] in terms of indirect combustion noise sources that originate from within the nozzle. In a large-eddy simulation of an underexpanded jet, Liu *et al*.[18] showed an aft noise lobe, in addition to the Mach wave radiation lobe, and ascribed this second lobe to the maximum contribution of the shock-associated noise. In Fig. 13 of Ref. [18] (cold jet) and Fig. 9d of Ref. [19] (heated jet), striation patterns were shown in the spatial/spectral domain of the source that resulted from the shock-cell noise component. In an NAH experiment of a high-speed, heated, laboratory-scale jet by Long *et al*.,[20] similar striations were shown to match the locations of shock cells when imaged at the source. The results of these studies and a previous NAH reconstruction of a full-scale jet[7] point toward shock cell interactions as a likely cause of multilobe radiation. Another possible contribution to the multilobe radiation pattern was suggested by Liu *et al*.[21] from simulations of a high-temperature, ideally expanded supersonic jet, free of shock cells. These simulations show that at high temperatures, two noise components exist and suggest that Mach wave radiation and large-scale turbulence radiation may be distinct phenomena, rather than two descriptors of the same source mechanism.

A frequency-dependent characterization of the multilobe radiation is obtained from NAH imaging of jet noise from a tethered F-35. In this paper, a brief discussion of the experimental setup describes the three acoustic arrays used for the hologram and benchmark verification of the NAH reconstruction. An advanced NAH method called multisource statistically optimized NAH (M-SONAH) was developed previously to incorporate the effects of multiple or spurious sources in a sound field.[22] This method can account for the presence of ground reflections the noise imaging of tethered, high-performance military aircraft and the application methods of M-SONAH to the F-35 data is described. Preliminary NAH reconstructions at 100% Engine Thrust Request are compared with benchmark measurements for both inward and outward propagation. Sound field images are presented, including a discussion of the multilobe nature of the F-35 sound field and evidence of broadband shock associated noise. The narrowband NAH reconstructions provide evidence that, while prior OTO spectra exhibited a transition between two peak frequencies, there are in fact more than two such transition frequencies. These results provide additional characterization of the multilobe phenomenon that needs to be accounted for in future modeling efforts.

II. Experiment

An extensive measurement of F-35A and F-35B acoustic emissions was performed at Edwards Air Force Base in 2013.[23] Each aircraft was tethered to a concrete run-up pad (see Fig. 1(a)). The engine was cycled through various engine powers from the lowest power setting of approximately 13% Engine Thrust Request (ETR), also called IDLE, up through the highest setting of 150% ETR. Each variant of the F-35 had a Pratt & Whitney F135 afterburning turbofan engine, which can achieve up to 43,000 pounds of thrust. The engine had a round nozzle that was approximately 1 m in diameter, but the nozzle size changed as a function of engine power. The nozzle center was 2 m from the ground.

The coordinate system relative to the aircraft is shown in Fig. 1(b). The distance downstream of the nozzle is represented by z, the perpendicular distance from the jet centerline by x, and the distance above the ground by y. This coordinate system is different than the one used in a previous report of measured F-35 field levels based on the same dataset[23] but is consistent with the coordinates used in previous full-scale imaging studies.[6,7] To facilitate this consistency, the figures shown herein are mirror images of the physical reality of the measurement. Polar angles are shown with respect to the direction forward from the aircraft nose (inlet axis), and are centered on a point called the microphone array reference point (MARP) that was 6.6 m behind the nozzle for the F-35A (7.5 m for the F-35B).

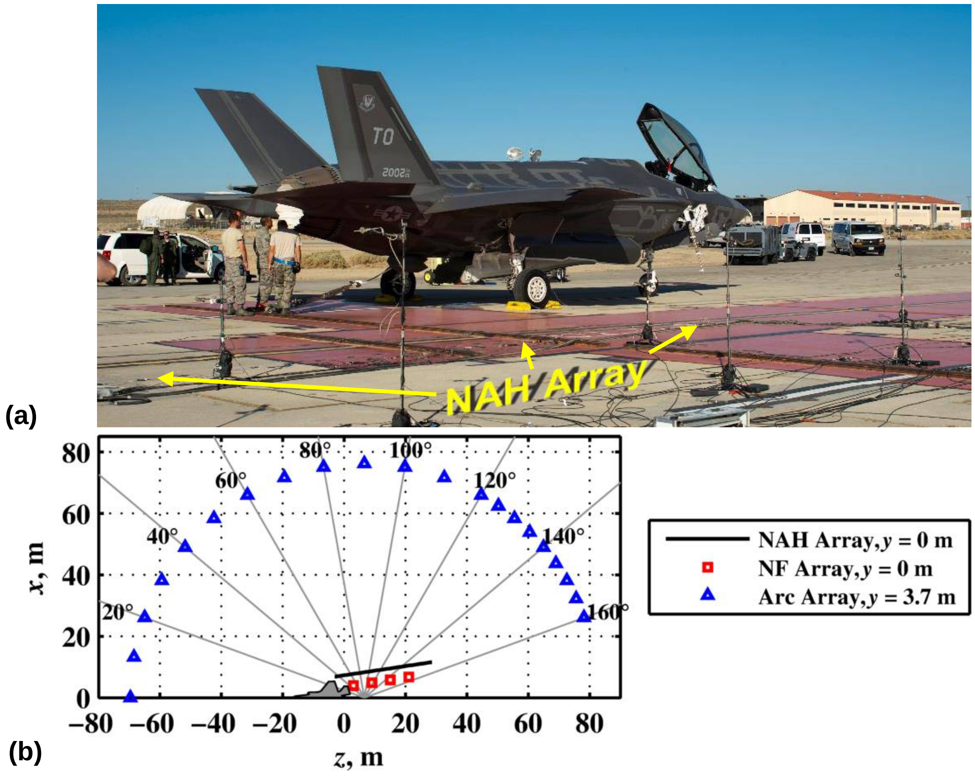

Figure 1. (a) Photograph of the F-35 aircraft (mirror image). (b) Schematic of the measurement locations relative to the aircraft.

A large number of microphones were deployed from the extreme near field to over 1200 m from the aircraft during measurements. For the purposes of this paper, three microphone arrays are discussed. First, a linear microphone array designed for NAH was placed along the ground with 0.45-m spacing, which spanned 32 m along the length of the jet (a total of 71 microphones), as shown in Fig. 1(b) by a black line. This NAH array was approximately parallel to jet shear layer boundary. The second array, called the near-field (NF) array (red squares in Fig. 1(b)), contained four microphones on the ground and was closer to the jet than the NAH array. Lastly, an arc of microphones with a radius of 76 m and centered on the MARP was placed at a height of $y = 3.7$ m above the ground. Data from the NF and arc arrays are compared to NAH reconstructions, as validation of the method, in Section IV.

III. Imaging Methods

Because the aircraft noise was measured in the presence of a rigid ground surface, the effects of the reflections must be incorporated into the NAH algorithm. The underlying source model assumed in the NAH method is an equivalent wave model (EWM) of the sound field consisting of two sets of cylindrical wave functions, one centered on the jet centerline and a second centered on the reflected image of the centerline. An advanced NAH algorithm called multisource statistically optimized NAH (M-SONAH) was developed to accommodate such models[22] and was validated in a previous full-scale jet noise analysis.[7]

M-SONAH is applied here to the F-35 ground array data, and the sound field near field the aircraft is reconstructed. The method of implementing M-SONAH on the full-scale jet data proceeds as follows.

1) Extract frequency-dependent complex pressures from recorded pressure waveforms.
2) Perform a partial field decomposition (PFD) to generate mutually incoherent partial fields.
3) Numerically extrapolate each partial field beyond the measurement aperture.
4) Formulate the EWM of the jet in the run-up pad environment.
5) Project the pressures of each partial field to desired locations.
6) Sum the projected partial fields energetically.

Each of these steps is explained in more detail.

First, the frequency-dependent complex pressures are obtained for all locations and engine conditions. The recorded time signals are split into blocks with 50% overlap and windowed with a Hanning function, then the Fourier transform is applied to each block to give complex pressures. The remainder of the processing is performed on selected narrowband frequencies independently. For each selected frequency, the input hologram is defined as the complex pressures for the different blocks across the NAH array.

This input hologram, however, is not necessarily self-coherent – a requirement in an NAH algorithm. Hence, for the second step, a PFD based on singular value decomposition (SVD)[24] of the input hologram is performed that results in a collection of self-coherent, but mutually incoherent, partial fields. Steps 3-5 are performed independently on each partial field; the partial fields were summed to obtain the total fields in step 6.

The SONAH algorithm[25] was originally developed in part to relax the requirement for a measurement aperture that extends far beyond the edges of a source, as is required in conventional NAH. Thus, at least when the standoff distance of the hologram from the source is very small, SONAH reconstruction artifacts from the data truncation at the edges are insignificant. For the current experiment, the aperture was limited by the fact that transducers could not be placed closer than several meters to the aircraft and even the 32-m aperture was not sufficient to capture all of the downstream radiation from the extended jet noise source for the lowest frequencies. In addition, the relatively large propagation distances would result in significant edge-related artifacts if the measured hologram data were used directly. To mitigate the effects of aperture limitations, the third step is to numerically extrapolate the hologram partial fields.

In preparation for this work, several extrapolation methods were investigated for their ability to represent physically realistic data immediately outside of the measurement aperture.[26] Linear forward prediction was chosen for its relatively high accuracy in numerical experiments and its computational efficiency.

In linear forward prediction,[27] the coefficients of a polynomial are determined from existing data, and the polynomial is then used to predict data beyond the original aperture. In the current study, the complex pressure data along the partial field are used to determine the coefficients of the polynomial, and the value of the polynomial immediately beyond the last point of the row is taken as the first data point outside the aperture. Then, the entire row of data, including the first extrapolated point, is used to find a polynomial and predict the second extrapolated point. This process is repeated to extend the aperture about 20 m in both the upstream and downstream directions for all partial fields. Then, a Tukey window is applied to the extended data to reduce reconstruction artifacts that result from non-physical predictions far from the measurement aperture edge. The Tukey window is defined to have a value of 1 at the measurement aperture edge and to decay to 0 within 1 acoustic wavelength.

Fourth, the EWM used in the M-SONAH algorithm is formulated to represent the jet in the presence of the ground reflection. As described in Ref. [22], the EWM includes one set of cylindrical wave functions centered on the jet centerline and a second set centered on the image source created by the reflection. Cylindrical wave functions for outward propagating waves are defined as

$$\Phi_{\ell,k_z}(r,\phi,z) \equiv \frac{H_\ell^{(1)}(k_r r)}{H_\ell^{(1)}(k_r r_0)} e^{i\ell\phi} e^{ik_z z}, \quad r \geq r_0 \tag{1}$$

where r, ϕ, and z are the radial, azimuthal, and axial spatial coordinates, respectively; $H_\ell^{(1)}$ is the ℓth-order Hankel function of the first kind; i represents the imaginary unit; r_0 is some small reference radius (traditionally the assumed source radius);[28] and k_z is the axial wavenumber. The radial wavenumber, k_r, is then constrained by

$$k_r = \begin{cases} \sqrt{k^2 - k_z^2}, & \text{for } |k| \geq |k_z|\,, \\ i\sqrt{k_z^2 - k^2}, & \text{for } |k| < |k_z|\,, \end{cases} \tag{2}$$

where $k = \omega/c$ is the acoustic wavenumber, ω is the angular frequency, and c is the speed of sound.

Two wave function sets are chosen to represent the jet source and its image in the EWM. The wave function sets are defined in Table 1, along with the necessary equations to transform from the Cartesian coordinates of Figure 1(b) to the respective coordinates used in each wave function, and the orders and coordinate-specific wave numbers included in each set. The vector $\mathbf{r} = (r,\phi,z)$ in Table 1 represents a local coordinate in the respective wave function set, with $r = 0$ being the centerline of the jet (or the centerline of the reflected image source). In cartesian coordinates, the jet centerline is at $x = 0$ m, $y = 2$ m, and the image centerline is $x = 0$ m, $y = -2$ m. The vector $\mathbf{r}_h$ corresponds to positions of the set of hologram points (after aperture extension), and $\mathbf{r}_q$ is the set of locations at which the sound field is to be reconstructed. Thus, $\mathbf{B}_1$ and $\mathbf{B}_2$ are the hologram wave function matrices for the jet and image sources, respectively, and $\boldsymbol{\beta}_1$ and $\boldsymbol{\beta}_2$ are the respective reconstruction matrices. In Table 1, the wavenumber spacing, Δk_z, and the wavenumber extrema, $|k_z|_{\max}$, are specified by the axial aperture length, L_z, and the axial sample spacing, Δz, according to the recommendations of Hald.[2] Each wave function matrix has a number of rows equal to the number of wave functions and a number of columns equal to the number of hologram or reconstruction points. The total EWM matrices are formed by concatenating the two sets of wave functions for the hologram and reconstruction locations, respectively, as

$$\mathbf{A} = \begin{bmatrix} \mathbf{B}_1 \\ \mathbf{B}_2 \end{bmatrix}, \text{and } \boldsymbol{\alpha} = \begin{bmatrix} \boldsymbol{\beta}_1 \\ \boldsymbol{\beta}_2 \end{bmatrix}. \tag{3}$$

Table 1 Definition of two wave function sets designed to represent a jet source and its image source.

$\mathbf{B}_1 \equiv [\Phi_{\ell,k_z}(\mathbf{r}_h)]$ and $\boldsymbol{\beta}_1 \equiv [\Phi_{\ell,k_z}(\mathbf{r}_q)]$, where $r \equiv \sqrt{x^2 + (y - 2\text{ m})^2}$ $\phi \equiv \tan^{-1}\left(\frac{y-2\text{ m}}{x}\right)$, fourth-quadrant arctangent with range $(-\pi,\pi]$ $z \equiv z$ $\ell = 0$ $\Delta k_z = \pi/L_z$, $\|k_z\|_{\max} = 2\pi/\Delta z$
$\mathbf{B}_2 \equiv [\Phi_{\ell,k_z}(\mathbf{r}_h)]$ and $\boldsymbol{\beta}_2 \equiv [\Phi_{\ell,k_z}(\mathbf{r}_q)]$, where $r \equiv \sqrt{x^2 + (y + 2\text{ m})^2}$ $\phi \equiv \tan^{-1}\left(\frac{y+2\text{ m}}{x}\right)$, fourth-quadrant arctangent with range $(-\pi,\pi]$ $z \equiv z$ $\ell = 0$ $\Delta k_z = \pi/L_z$, $\|k_z\|_{\max} = 2\pi/\Delta$

For this analysis, only the azimuthal order $\ell = 0$ is included, because the EWM is restricted to the axisymmetric mode. The limited azimuthal coverage of the measurement made the representation of higher orders inaccurate. This does not mean that higher orders are not important to model the jet, only that the array did not accurately capture them. However, the axisymmetric source assumption combined with the ground reflection in the EWM seems to have captured salient features of the interference pattern[8] that are essential for modeling how the source behaves in the presence of the ground reflection. Additional investigations will be performed to investigate these assumptions further.

With the EWM defined, the fifth step of sound field propagation was performed. At this point, the M-SONAH processing becomes identical to, SONAH.[2] The projected pressures at the reconstruction locations are

$$\mathbf{p}(\mathbf{r}_q) = \mathbf{p}^{\mathrm{T}}(\mathbf{r}_h)\mathbf{R}_{\mathbf{A}^{\mathrm{H}}\mathbf{A}}\,\mathbf{A}^{\mathrm{H}}\boldsymbol{\alpha}\,, \tag{4}$$

where superscript H is the Hermitian transpose, $\mathbf{p}^{\mathrm{T}}(\mathbf{r}_h)$ is the transpose of the complex pressures on the hologram, and $\mathbf{R}_{\mathbf{A}^{\mathrm{H}}\mathbf{A}}$ is the regularized inverse of $\mathbf{A}^{\mathrm{H}}\mathbf{A}$. Regularization was performed using the modified Tikhonov filter in conjunction with the generalized cross-validation (GCV) procedure for the selection of the regularization parameter.[29]

In the concluding step, the squared pressures of all partial fields are summed to obtain the magnitude of the total pressure field. All the levels shown in dB here are scaled to represent the levels extracted for select frequencies from a power spectral density.

IV. Results

As a preliminary result, the input hologram of the F-35A at 100% ETR engine power is used in M-SONAH to reconstruct the sound field. Level differences between the F-35A and F-35B were typically less than 1 dB, so it is expected that source characteristics for the F-35B would be similar to those shown here. The first part of this section compares field M-SONAH reconstructions to measured benchmark levels at the NF and arc arrays. The second part shows two-dimensional field reconstruction maps in the jet vicinity and discusses source and radiation characteristics.

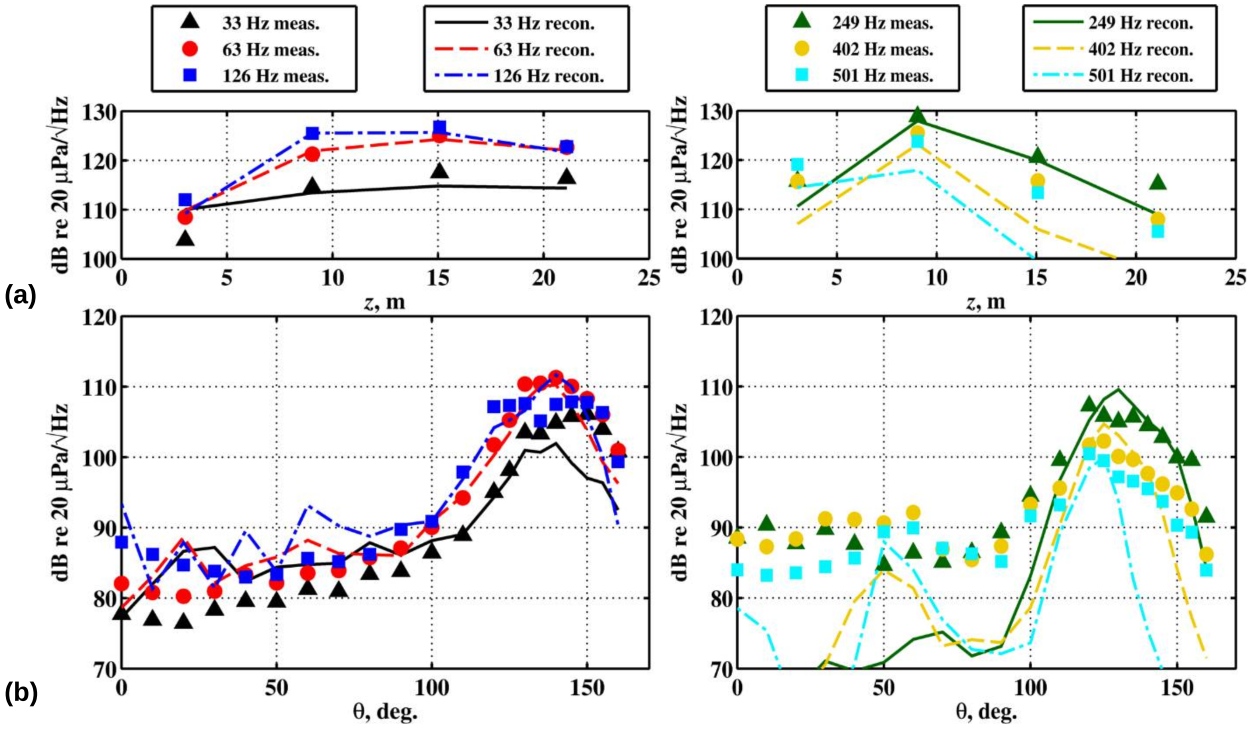

Figure 2. Comparison of reconstructed narrowband spectral density levels to measured benchmark levels for select frequencies from 33 to 501 Hz (a) at the four ground microphones closest to the jet and (b) along the 76 m arc.

Validation of the M-SONAH field reconstructions is shown via comparison with measured levels at six frequencies from 33 to 501 Hz. The ideal validation of the ground reflection model would include comparison of reconstructions to data points sampled vertically in high resolution. Such data were not collected in this measurement, but the two arrays selected for the benchmark comparison herein were located at different heights: one on the ground and one 3.7 m above the ground.

Inward reconstructions at the location of the NF array are shown in Fig. 2(a). Note that differences between reconstructions (symbols) and benchmarks (lines) are less than about 2 dB for most locations at 33 - 249 Hz. At 249 Hz, the differences are larger near the aperture edges ($z = 3$ m and $z = 21$ m), and these edge errors grow with increasing frequency. This is partially due to the fact that, for the highest frequencies, there were fewer than two microphones per acoustic wavelength (the theoretical "Nyquist" limit for the array spacing is 375 Hz). However, at the location corresponding to largest measured level (near $z = 8$ m) the difference between reconstructed and measured levels is 0 dB at 249 Hz, 2 dB at 402 Hz, and 4 dB at 501 Hz, because the primary radiation energy for all frequencies was obliquely incident on the array, so the two-microphone-per-wavelength criterion was met for the trace wavelength along the array.[30] This comparison provides evidence that the M-SONAH successfully reconstructs levels closer to the aircraft than the NAH array within the limitations of the array.

Overall, the outward reconstructions to the 76-m arc, shown in Fig. 2(b), match the measured levels and spatial trends in the far field. At 33, 63 and 126 Hz, the reconstructed levels (lines) follow the same trends as the measured levels (symbols) with a few exceptions. First, the underestimation of the maximum level near 150˚ for 33 Hz is likely due to the limited spatial extent of the NAH array and the far-downstream directivity of the lowest frequencies. Second, the oscillatory behavior in the reconstructions at 126 Hz is due to the windowing effects from a finite measurement aperture, which is common in the low-amplitude regions of NAH reconstructions. At 249, 402 and 501 Hz, the maxima in the reconstructed levels are within 2-3 dB of the measured levels and occur within 0° to 10° of the maximum angles. Away from the dominant radiation direction, the reconstructions underestimate the levels—an effect that becomes more pronounced with increasing frequency. This underestimation may occur because of low spatial coherence of the sound field of the array and the reduced-order "filtering" that occurs during the PFD process. Further investigations are necessary to confirm this and correct the limitation.

It is interesting that the low-frequency level reconstructions (33-126 Hz of Fig. 2(b)) are within 5 to 10 dB of the benchmark as far forward as 0˚ (See Fig. Figure 1(b)), even though the NAH array only extended to roughly 40˚ upstream. The jet noise sources for these frequencies originated from regions about 15+ m downstream of the nozzle, which may result in an extended effective upstream coverage by the NAH array. It is also possible that the underestimations typical of insufficient array aperture coverage are countered by the shielding effects of the aircraft body in the forward direction. Additional verifications are necessary before the current M-SONAH reconstruction can be used to model the forward radiation.

Another important feature of the far-field reconstruction is the presence of a distinct local maximum in the forward direction (around 50˚) for 402 and 501 Hz in Fig. 2(b). Such a local maximum does not exist at the lower frequencies, which is behavior consistent with broadband shock-associated noise (BSAN). The appearance of the maxima at 50˚ in the reconstructions—approximately 10-20 dB above the surrounding levels—indicate this noise feature has high coherence (again consistent with BSAN). The fact that the levels are much closer to the benchmark measurement at 50˚ than the surrounding levels suggests that the hologram may have contained sufficient information about this noise feature. The local maximum is less distinct in the benchmark measurement, suggesting that BSAN may be a highly coherent feature that is dominated or overshadowed by less coherent fine-scale turbulence radiation in the forward direction.

The comparisons between the reconstructions and measurement shown in Figure 2 give an indication of the performance of M-SONAH when used to reconstruct the three-dimensional sound field around the aircraft. The reconstructed fields at a height of $y = 0$ m are displayed in Figure 3 for the same six frequencies shown previously. The white line indicates the location of the NAH array. In the far field, the dominant radiation lobes swing forward as frequency increases. Note also the presence of a narrow, low-amplitude lobe, attributed to BSAN, radiating in the forward direction for 402 and 501 Hz, consistent with the directivities shown in Fig. 2(b). The reconstruction levels near the jet centerline ($x = 0$ m) correspond to an M-SONAH-derived, frequency-dependent equivalent source model of pressure distributions that contract and move upstream as frequency increases. These preliminary reconstructions demonstrate the potential of M-SONAH in equivalent source modeling and field prediction efforts.

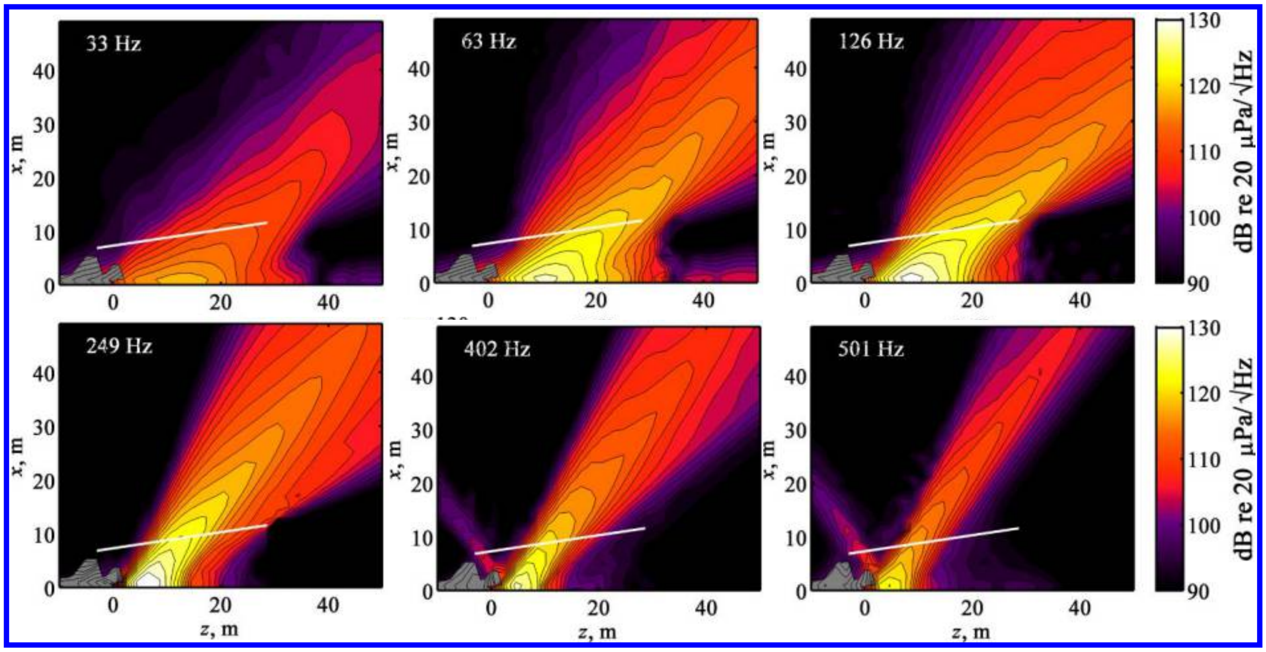

Figure 3. M-SONAH reconstruction of narrowband spectral density levels on the ground with the F-35 operating at 100% ETR for select frequencies from 33 to 501 Hz.

The M-SONAH field reconstructions also provide the opportunity to probe F-35 multilobe radiation. A dual-lobe in the level measured in the vicinity of a high-performance military aircraft operating at high engine powers was previously described in Refs. [8] and [31]. Since then, this feature has been hypothesized to arise from shock-cell/turbulent structure interactions,[7] the separation of Mach wave radiation from large-scale turbulence radiation,[32] and internal combustion noise.[17] The prior full-scale jet noise was reported in terms of one-third octave band spectral levels showed only two lobes, but the narrowband power spectral densities (PSD) for the F-35A, shown in Fig. 4, indicate that there are more than two lobes. The PSD as a function of distance *z* along the NAH array reveal the presence of three distinct local maxima near the frequency/location pairs of (100 Hz, 20 m), (230 Hz, 13 m), and (350 Hz, 10 m), with a less distinct fourth maximum near (475 Hz, 9 m). Prior hypotheses about the cause of the dual-lobe feature need to be reevaluated in light of these additional peaks.

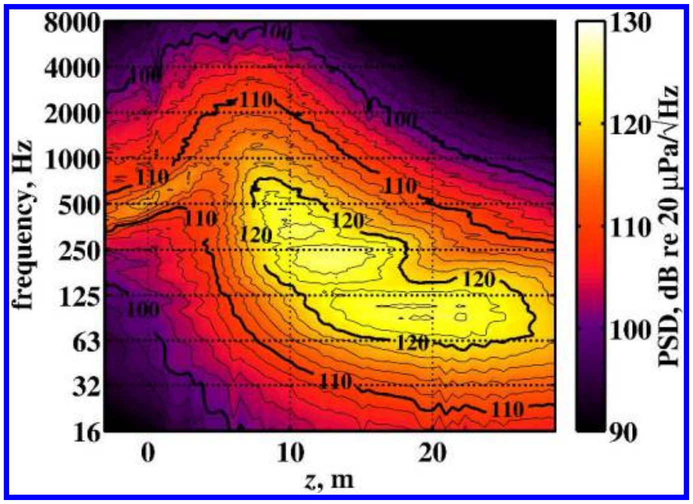

Figure 4. Spatio/spectral maps of the PSD measured across the NAH array.

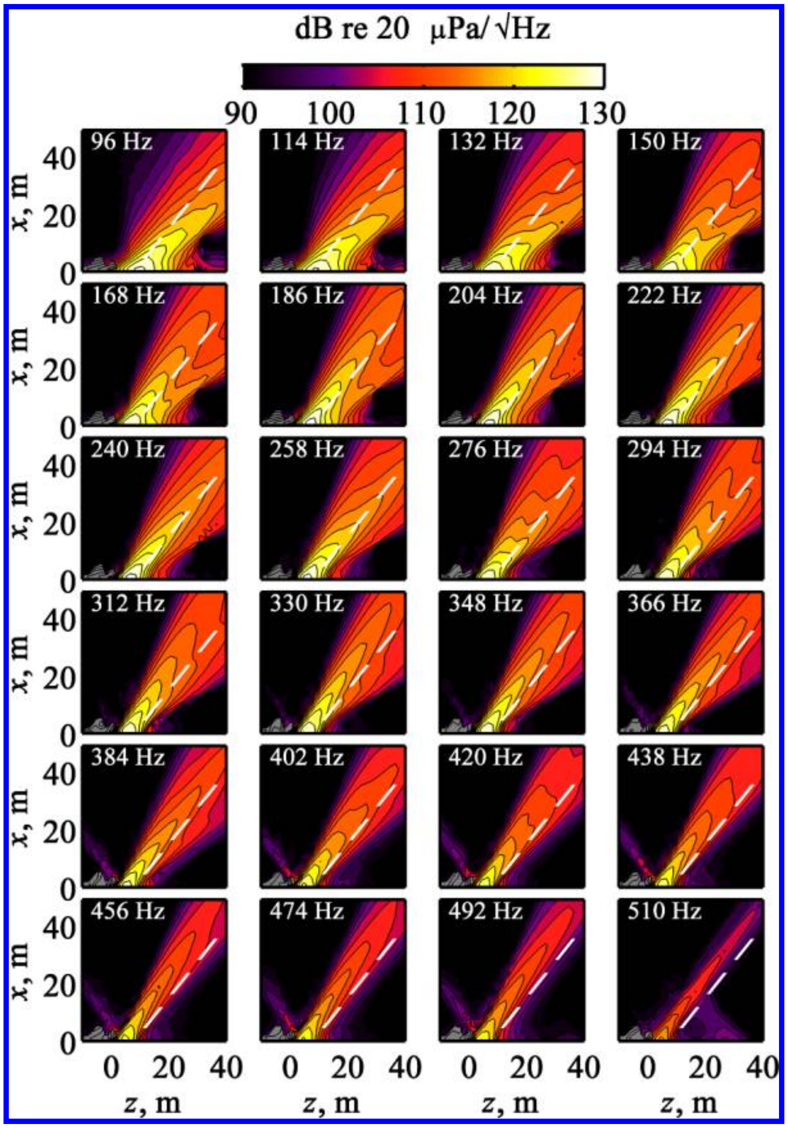

Figure 5. M-SONAH reconstruction of power density levels on the ground for a set of densely spaced narrowband frequencies.

The spatial/spectral behavior of these multiple lobes is clarified by examining reconstructed power spectral density levels for narrowband frequencies from 96 to 510 Hz, with 18-Hz resolution. M-SONAH reconstructions over the $y = 0$ m plane in Fig. 5 predict how the sound radiation changes with frequency. The dashed line on each sound map does not have physical significance; it is a spatial reference point at the same location on each map to facilitate multilobe comparisons across frequencies. The two lowest frequencies (96 and 114 Hz) show a single dominant lobe. As frequency increases from 132 to 168 Hz, this lobe gradually swings more toward the aft direction, and a second lobe emerges at a slightly lower angle (upstream). From 186 to 222 Hz, the first lobe diminishes. The second lobe swings aft with increasing frequency, and a third lobe emerges just upstream of the second from 258 to 294 Hz. Then the second lobe diminishes from 312 to 330 Hz. Finally, a fourth lobe emerges upstream of the third between 384 and 420 Hz (still in the aft direction, not to be confused with the BSAN lobe pointing in the forward direction), although it is less distinct than the previous three. At 456 Hz and above, the third lobe has diminished and all features of the primary radiation exist in a single, merged lobe. Comparison of reconstructions from 96 Hz to 510 Hz in Fig. 5 shows that the *overall* primary radiation shifts gradually in the forward direction with increasing frequency, but each lobe independently shifts aft with increasing frequency. It is possible that this behavior is due to the interaction of turbulent structures with regularly spaced shock-cell boundaries.[20] However, unlike the laboratory-scale studies where direct connections can be made between localized acoustic source maxima and shock cell boundaries,[18-20] the full-scale lobes shown in Fig. 5 coalesce in the vicinity of the source, precluding a one-to-one correlation of lobe origins to individual shock cells. Alternative investigations may be required to validate this connection, but the radiated field behavior is consistent with the laboratory-scale phenomenon.

The M-SONAH reconstructions shown in Figure 5 demonstrate the frequency dependence of the distinct local maximum at 50˚ attributed to BSAN in the discussion of Figure 2. The BSAN radiation lobe is present at frequencies as low as 330 Hz, and while not seen clearly in Fig. 5, it is visible as high as 501 Hz (See Fig. 3.). The spatially dependent spectra in Figure 4 show that the BSAN directivity shifts aft with increasing frequency, similar to the behavior of each multilobe component as discussed above. This further supports the idea that the multilobe behavior was a result of shock-cell interactions.

In the reconstructions at 510 Hz in Fig. 5, there is a strong downstream feature along the jet centerline with what appears to be a forward radiation directivity. This is actually an aliasing artifact of the NAH processing due to the inability of the array to distinguish forward and aft waves at and above 510 Hz given the resolution of the array and the trace wavelength of the sound waves present in this field. Efforts are underway to create a refined model of the phase information measured along the array in order to extend the NAH reconstructions to higher frequencies.

V. Concluding Discussion

The application of M-SONAH on a hologram near the F-35A has led to insights into the spatially dependent spectral characteristics of the jet noise sources. M-SONAH field reconstructions were obtained for a tethered F-35A operating at 100% ETR. A comparison of both inward and outward field reconstructions to measured benchmarks has demonstrated a preliminary verification of the reconstruction accuracy and helped to define an upper frequency limit of about 510 Hz for which accurate results can be achieved for the current processing methods. Reconstruction results have also provided evidence of a highly self-coherent BSAN lobe, above 300 Hz, within an incoherent field, radiating in the forward direction.

The frequency-dependent trends of the reconstructions also shed light into the behavior of what was previously referred to as “the dual lobe” or the “double spectral peak” in high performance, military aircraft noise. While prior investigations have shown evidence of a spatially dependent dual lobe in the one-third octave band spectra[8,9,23] and NAH reconstructions,[7,10] this paper contains the first narrowband evidence that there are more than two lobes in the noise from a high-performance military aircraft. The narrowband jet noise from the F-35A contains clear multilobe behavior in which the spectral peaks appears to shift between 100, 230, 350, and 475 Hz across the 32-m aperture spanned by the NAH array. As frequency increases, each lobe moves aft and decreases in amplitude as a subsequent lobe located in a more forward direction emerges; the directivity of each lobe moves farther aft with increasing frequency while the overall directivity moved forward with increasing frequency. These details may not visible with OTO processing as was required in past reconstructions of a full-scale jet[7,8,9,10] due to restrictions on the use of the data. Hence, it is possible that the double lobe discussed in these past studies is in fact a low-resolution representation of additional lobes.

In future work, advanced array processing techniques will be used to extend the window of accurate reconstructions to higher frequencies. This will allow a more complete characterization of BSAN radiation, the multilobe radiation, and fine-scale turbulence radiation in regions away from the dominant main-radiation lobes. In addition, advanced partial field decomposition methods[10,33] will be employed to isolate independent radiators that generate the multilobe radiation.

Acknowledgments

SBIR DATA RIGHTS - (DFARS 252.227-7018 (JUNE 1995)); Contract Number: FA8650-08-C-6843; Contractor Name & Address: Blue Ridge Research and Consulting, LLC, 29 N Market St, Suite 700; Asheville, NC; Expiration of SBIR Data Rights Period: May 2, 2021 (Subject to SBA SBIR Directive of September 24, 2002). *The Government's rights to use, modify, reproduce, release, perform, display, or disclose technical data or computer software marked with this legend are restricted during the period shown as provided in paragraph (b)(4) of the Rights in Noncommercial Technical Data and Computer Software—Small Business Innovation Research (SBIR) Program clause contained in the above identified contract. No restrictions apply after the expiration date shown above. Any reproduction of technical data, computer software, or portions thereof marked with this legend must also reproduce the markings.*

References

[1]Maynard, J. D., Williams, E. G., and Lee, Y., “Nearfield acoustic holography: 1. Theory of generalized holography and the development of NAH,” *J. Acoust. Soc. Am.*, Vol. 78, 1985, pp. 1395–1413.

[2] Hald, J., “Basic theory and properties of statistically optimized near-field acoustical holography,” *J. Acoust. Soc. Am.*, Vol. 125, 2009, pp. 2105–2120.

[3]Lee, M., and Bolton, J. S. , “Source characterization of a subsonic jet by using near-field acoustical holography,” *J. Acoust. Soc. Am.*, Vol. 121, 2007, pp. 967–977.

[4]Long, D. F., “Jet noise source location via acoustic holography and shadowgraph imagery,” AIAA Paper 2008–2888, 2008.

[5]Shah, P. N., Vold, H., and Yang, M., “Reconstruction of far-field noise using multireference acoustical holography measurements of high-speed jets,” AIAA Paper 2011-2772, 2011.

[6]Wall, A. T., Gee, K. L., Neilsen, T. B., Krueger, D. W., and James, M. M., “Cylindrical acoustical holography applied to full-scale jet noise,” *J. Acoust. Soc. Am.*, Vol. 136, 2014, pp. 1120–1128.

[7]Wall, A. T., Gee, K. L., Neilsen, T. B., McKinley, R. L., and James, M. M., “Military jet noise source imaging using multisource statistically optimized near-field acoustical holography,” *J. Acoust. Soc. Am.*, Vol. 139, 2016, pp. 1938-1950.

[8]Wall, A. T., Gee, K. L., James, M. M., Bradley, K. A., McInerny, S. A., and Neilsen, T. B., “Near-field noise measurements of a high-performance military jet aircraft," *Noise Control Eng. J.*, Vol. 60, 2012, pp. 421-434.

[9]Neilsen, T. B., Gee, K. L., Wall, A. T., and James, M. M., “Similarity spectra analysis of high-performance jet aircraft noise,” *J. Acoust. Soc. Am.*, Vol. 133, 2013, pp. 2116–2125.

[10]Wall, A. T., Gee, K. L., Neilsen, T. B., Harker, B. M., McInerny, S. A., McKinley, R. L., and James, M. M., “Investigation of multi-lobed fighter jet noise sources using acoustical holography and partial field decomposition methods,” AIAA Paper 2015-2379, 2015.

[11]Mollo-Christensen, E., “Jet noise and shear flow instability seen from an experimenter’s viewpoint,” *J. Applied Mech.*, Vol. 34, 1967, pp. 1–7.

[12]Tam, C. K. W., “Directional acoustic radiation from a supersonic jet generated by shear layer instability,” *J. Fluid Mech.*, Vol. 46, 1971, pp. 757-768.

[13]Tam, C. K. W., “Mach wave radiation from high-speed jets," *AIAA J.*, Vol. 47, 2009, pp. 2440-2448.

[14]Schlinker, R. H., Liljenberg, S. A., Polak, D. R., Post, K. A., Chipman, C. T., and Stern, A. M., “Supersonic jet noise source characteristics & propagation: Engine and model scale," AIAA Paper 2007-3623, 2007.

[15]Greska, B., and Krothapalli, A., “On the far-field propagation of high-speed jet noise,” *Proceedings of NCAD / NoiseCon 2008*, NCAD2008-73071, American Society of Mechanical Engineers, 2008.

[16]Norum, T. D., Garber, D. P., Golub, R. A., Santa Maria, O. L., and Orme, J. S., “Supersonic Jet Exhaust Noise at High Subsonic Flight Speed,” NASA/TP-2004-212686, 2004.

[17]Tam, C. K. W., and Parrish, S. A., “Noise of high-performance aircraft at afterburner,” *J. Sound Vib.*, Vol. 352, 2015, pp. 103-208.

[18]Liu, J., Corrigan, A., Kailasanath, K., and Gutmark, E., “Impact of chevrons on noise source characteristics in imperfectly expanded jet flows,” AIAA Paper 2015-2835, 2015.

[19]Liu, J., Kailasanath, K., and Gutmark, E., “Similarity Spectral Analysis of Highly Heated Supersonic Jets Using Large-Eddy Simulations,” AIAA Paper 2017-0926, 2017.

[20]Long, D. F., “Jet noise source location via acoustic holography and shadowgraph imagery,” AIAA Paper 2008-2888, 2008.

[21]Liu, J., Corrigan, A., Kailasanath, K., and Taylor, B., “Impact of the specific heat ratio on noise generation in a high-temperature supersonic jet,” AIAA Paper 2016-2125, 2016.

[22]Wall, A. T., Gee, K. L., and Neilsen, T. B., "Multisource statistically optimized near-field acoustical holography," *J. Acoust. Soc. Am.*, Vol. 137, 2015, pp. 963-975.

[23]James, M. M., Salton, A. R., Downing, J. M., Gee, K. L., Neilsen, T. B., Reichman, B. O., McKinley, R., Wall, A. T., and Gallagher, H., “Acoustic Emissions from F-35A and F-35B Aircraft during Ground Run-Up,” AIAA Paper 2015-2375, 2015.

[24]Hald, J., “STSF—A unique technique for scan-based nearfield acoustical holography without restriction on coherence,” Technical Report No. 1, from Bruel & Kjaer, Naerum, Denmark, 1989.

[25]Steiner, R., and Hald, J., “Near-field acoustical holography without the errors and limitations caused by the use of spatial DFT,” *Int. J. Acoust. Vib.*, Vol. 6, 2001, pp. 83-89.

[26]Wall, A. T., Gee, K. L., Krueger, D. W., Neilsen, T. B., Sommerfeldt, S. D., and James, M. M.. “Aperture extension for near-field acoustical holography of jet noise,” *Proc. Mtgs. Acoust.*, Vol. 14, 2013, p. 065001.

[27]Jackson, L. B., *Digital Filters and Signal Processing*, 2nd Ed., Kluwer Academic Publishers, Boston, 1989, pp. 255-257.

[28]Cho, Y. T., Bolton, J. S., and Hald, J., “Source visualization by using statistically optimized near-field acoustical holography in cylindrical coordinates,” *J. Acoust. Soc. Am.*, Vol. 118, 2005, 2355-2364.

[29]Williams, E. G., “Regularization methods for near-field acoustical holography," *J. Acoust. Soc. Am.*, Vol. 110, 2001, pp. 1976-1988.

[30]Wall, A. T., Gee, K. L., and Neilsen, T. B., “Modified statistically optimized near-field acoustical holography for jet noise characterization,” *Proc. Mtgs. Acoust.*, Vol. 19, 2013, p. 055013.

---

[31] Wall, A. T., Gee, K. L., Neilsen, T. B., Krueger, D. W., James, M. M., Sommerfeldt, S. D., and Blotter, J. D., "Full-Scale Jet Noise Characterization Using Scan-Based Acoustical Holography," AIAA Paper 2012-2081, 2012.

[32] Liu, J., Corrigan, A., Kailasanath, K., and Gutmark, E., "Effects of Temperature on Noise Generation in Supersonic Jets," AIAA Paper 2016-2937, 2016.

[33] Wall, A. T., Gee, K. L., Neilsen, T. B., and James, M. M., "Acoustical holography and proper orthogonal decomposition methods for the analysis of military jet noise," *Proc. Noise-Con 2013*.